Einstein@Home search for periodic gravitational waves in early S5 LIGO data

B. P. Abbott,[17] R. Abbott,[17] R. Adhikari,[17] P. Ajith,[2] B. Allen,[2,60] G. Allen,[35] R. S. Amin,[21] S. B. Anderson,[17]
W. G. Anderson,[60] M. A. Arain,[47] M. Araya,[17] H. Armandula,[17] P. Armor,[60] Y. Aso,[17] S. Aston,[46] P. Aufmuth,[16]
C. Aulbert,[2] S. Babak,[1] P. Baker,[24] S. Ballmer,[17] C. Barker,[18] D. Barker,[18] B. Barr,[48] P. Barriga,[59] L. Barsotti,[20]
M. A. Barton,[17] I. Bartos,[10] R. Bassiri,[48] M. Bastarrika,[48] B. Behnke,[1] M. Benacquista,[42] J. Betzwieser,[17]
P. T. Beyersdorf,[31] I. A. Bilenko,[25] G. Billingsley,[17] R. Biswas,[60] E. Black,[17] J. K. Blackburn,[17] L. Blackburn,[20] D. Blair,[59]
B. Bland,[18] T. P. Bodiya,[20] L. Bogue,[19] R. Bork,[17] V. Boschi,[17] S. Bose,[61] P. R. Brady,[60] V. B. Braginsky,[25] J. E. Brau,[53]
D. O. Bridges,[19] M. Brinkmann,[2] A. F. Brooks,[17] D. A. Brown,[36] A. Brummit,[30] G. Brunet,[20] A. Bullington,[35]
A. Buonanno,[49] O. Burmeister,[2] R. L. Byer,[35] L. Cadonati,[50] J. B. Camp,[26] J. Cannizzo,[26] K. C. Cannon,[17] J. Cao,[20]
L. Cardenas,[17] S. Caride,[51] G. Castaldi,[56] S. Caudill,[21] M. Cavaglià,[39] C. Cepeda,[17] T. Chalermsongsak,[17] E. Chalkley,[48]
P. Charlton,[9] S. Chatterji,[17] S. Chelkowski,[46] Y. Chen,[1,6] N. Christensen,[8] C. T. Y. Chung,[38] D. Clark,[35] J. Clark,[7]
J. H. Clayton,[60] T. Cokelaer,[7] C. N. Colacino,[12] R. Conte,[55] D. Cook,[18] T. R. C. Corbitt,[20] N. Cornish,[24] D. Coward,[59]
D. C. Coyne,[17] J. D. E. Creighton,[60] T. D. Creighton,[42] A. M. Cruise,[46] R. M. Culter,[46] A. Cumming,[48] L. Cunningham,[48]
S. L. Danilishin,[25] K. Danzmann,[2,16] B. Daudert,[17] G. Davies,[7] E. J. Daw,[40] D. DeBra,[35] J. Degallaix,[2] V. Dergachev,[51]
S. Desai,[37] R. DeSalvo,[17] S. Dhurandhar,[15] M. Díaz,[42] A. Dietz,[7] F. Donovan,[20] K. L. Dooley,[47] E. E. Doomes,[34]
R. W. P. Drever,[5] J. Dueck,[2] I. Duke,[20] J.-C. Dumas,[59] J. G. Dwyer,[10] C. Echols,[17] M. Edgar,[48] A. Effler,[18] P. Ehrens,[17]
G. Ely,[8] E. Espinoza,[17] T. Etzel,[17] M. Evans,[20] T. Evans,[19] S. Fairhurst,[7] Y. Faltas,[47] Y. Fan,[59] D. Fazi,[17] H. Fehrmann,[2]
L. S. Finn,[37] K. Flasch,[60] S. Foley,[20] C. Forrest,[54] N. Fotopoulos,[60] A. Franzen,[16] M. Frede,[2] M. Frei,[41] Z. Frei,[12]
A. Freise,[46] R. Frey,[53] T. Fricke,[19] P. Fritschel,[20] V. V. Frolov,[19] M. Fyffe,[19] V. Galdi,[56] J. A. Garofoli,[36] I. Gholami,[1]
J. A. Giaime,[21,19] S. Giampanis,[2] K. D. Giardina,[19] K. Goda,[20] E. Goetz,[51] L. M. Goggin,[60] G. González,[21]
M. L. Gorodetsky,[25] S. Goßler,[2] R. Gouaty,[21] A. Grant,[48] S. Gras,[59] C. Gray,[18] M. Gray,[4] R. J. S. Greenhalgh,[30]
A. M. Gretarsson,[11] F. Grimaldi,[20] R. Grosso,[42] H. Grote,[2] S. Grunewald,[1] M. Guenther,[18] E. K. Gustafson,[17]
R. Gustafson,[51] B. Hage,[16] J. M. Hallam,[46] D. Hammer,[60] G. D. Hammond,[48] C. Hanna,[17] J. Hanson,[19] J. Harms,[52]
G. M. Harry,[20] I. W. Harry,[7] E. D. Harstad,[53] K. Haughian,[48] K. Hayama,[42] J. Heefner,[17] I. S. Heng,[48] A. Heptonstall,[17]
M. Hewitson,[2] S. Hild,[46] E. Hirose,[36] D. Hoak,[19] K. A. Hodge,[17] K. Holt,[19] D. J. Hosken,[45] J. Hough,[48] D. Hoyland,[59]
B. Hughey,[20] S. H. Huttner,[48] D. R. Ingram,[18] T. Isogai,[8] M. Ito,[53] A. Ivanov,[17] B. Johnson,[18] W. W. Johnson,[21]
D. I. Jones,[57] G. Jones,[7] R. Jones,[48] L. Ju,[59] P. Kalmus,[17] V. Kalogera,[28] S. Kandhasamy,[52] J. Kanner,[49] D. Kasprzyk,[46]
E. Katsavounidis,[20] K. Kawabe,[18] S. Kawamura,[27] F. Kawazoe,[2] W. Kells,[17] D. G. Keppel,[17] A. Khalaidovski,[2]
F. Y. Khalili,[25] R. Khan,[10] E. Khazanov,[14] P. King,[17] J. S. Kissel,[21] S. Klimenko,[47] K. Kokeyama,[27] V. Kondrashov,[17]
R. Kopparapu,[37] S. Koranda,[60] D. Kozak,[17] B. Krishnan,[1] R. Kumar,[48] P. Kwee,[16] P. K. Lam,[4] M. Landry,[18] B. Lantz,[35]
A. Lazzarini,[17] H. Lei,[42] M. Lei,[17] N. Leindecker,[35] I. Leonor,[53] C. Li,[6] H. Lin,[47] P. E. Lindquist,[17] T. B. Littenberg,[24]
N. A. Lockerbie,[58] D. Lodhia,[46] M. Longo,[56] M. Lormand,[19] P. Lu,[35] M. Lubinski,[18] A. Lucianetti,[47] H. Lück,[2,16]
B. Machenschalk,[1] M. MacInnis,[20] M. Mageswaran,[17] K. Mailand,[17] I. Mandel,[28] V. Mandic,[52] S. Márka,[10] Z. Márka,[10]
A. Markosyan,[35] J. Markowitz,[20] E. Maros,[17] I. W. Martin,[48] R. M. Martin,[47] J. N. Marx,[17] K. Mason,[20] F. Matichard,[21]
L. Matone,[10] R. A. Matzner,[41] N. Mavalvala,[20] R. McCarthy,[18] D. E. McClelland,[4] S. C. McGuire,[34] M. McHugh,[23]
G. McIntyre,[17] D. J. A. McKechan,[7] K. McKenzie,[4] M. Mehmet,[2] A. Melatos,[38] A. C. Melissinos,[54] D. F. Menéndez,[37]
G. Mendell,[18] R. A. Mercer,[60] S. Meshkov,[17] C. Messenger,[2] M. S. Meyer,[19] J. Miller,[48] J. Minelli,[37] Y. Mino,[6]
V. P. Mitrofanov,[25] G. Mitselmakher,[47] R. Mittleman,[20] O. Miyakawa,[17] B. Moe,[60] S. D. Mohanty,[42] S. R. P. Mohapatra,[50]
G. Moreno,[18] T. Morioka,[27] K. Mors,[2] K. Mossavi,[2] C. MowLowry,[4] G. Mueller,[47] H. Müller-Ebhardt,[2] D. Muhammad,[19]
S. Mukherjee,[42] H. Mukhopadhyay,[15] A. Mullavey,[4] J. Munch,[45] P. G. Murray,[48] E. Myers,[18] J. Myers,[18] T. Nash,[17]
J. Nelson,[48] G. Newton,[48] A. Nishizawa,[27] K. Numata,[26] J. O'Dell,[30] B. O'Reilly,[19] R. O'Shaughnessy,[37] E. Ochsner,[49]
G. H. Ogin,[17] D. J. Ottaway,[45] R. S. Ottens,[47] H. Overmier,[19] B. J. Owen,[37] Y. Pan,[49] C. Pankow,[47] M. A. Papa,[1,60]
V. Parameshwaraiah,[18] P. Patel,[17] M. Pedraza,[17] S. Penn,[13] A. Perreca,[46] V. Pierro,[56] I. M. Pinto,[56] M. Pitkin,[48]
H. J. Pletsch,[2] M. V. Plissi,[48] F. Postiglione,[55] M. Principe,[56] R. Prix,[2] L. Prokhorov,[25] O. Punken,[2] V. Quetschke,[47]
F. J. Raab,[18] D. S. Rabeling,[4] H. Radkins,[18] P. Raffai,[12] Z. Raics,[10] N. Rainer,[2] M. Rakhmanov,[42] V. Raymond,[28]
C. M. Reed,[18] T. Reed,[22] H. Rehbein,[2] S. Reid,[48] D. H. Reitze,[47] R. Riesen,[19] K. Riles,[51] B. Rivera,[18] P. Roberts,[3]
N. A. Robertson,[17,48] C. Robinson,[7] E. L. Robinson,[1] S. Roddy,[19] C. Röver,[2] J. Rollins,[10] J. D. Romano,[42] J. H. Romie,[19]
S. Rowan,[48] A. Rüdiger,[2] P. Russell,[17] K. Ryan,[18] S. Sakata,[27] L. Sancho de la Jordana,[44] V. Sandberg,[18] V. Sannibale,[17]
L. Santamaría,[1] S. Saraf,[32] P. Sarin,[20] B. S. Sathyaprakash,[7] S. Sato,[27] M. Satterthwaite,[4] P. R. Saulson,[36] R. Savage,[18]
P. Savov,[6] M. Scanlan,[22] R. Schilling,[2] R. Schnabel,[2] R. Schofield,[53] B. Schulz,[2] B. F. Schutz,[1,7] P. Schwinberg,[18] J. Scott,[48]

042003-1

S. M. Scott,[4] A. C. Searle,[17] B. Sears,[17] F. Seifert,[2] D. Sellers,[19] A. S. Sengupta,[17] A. Sergeev,[14] B. Shapiro,[20]
P. Shawhan,[49] D. H. Shoemaker,[20] A. Sibley,[19] X. Siemens,[60] D. Sigg,[18] S. Sinha,[35] A. M. Sintes,[44] B. J. J. Slagmolen,[4]
J. Slutsky,[21] J. R. Smith,[36] M. R. Smith,[17] N. D. Smith,[20] K. Somiya,[6] B. Sorazu,[48] A. Stein,[20] L. C. Stein,[20]
S. Steplewski,[61] A. Stochino,[17] R. Stone,[42] K. A. Strain,[48] S. Strigin,[25] A. Stroeer,[26] A. L. Stuver,[19] T. Z. Summerscales,[3]
K.-X. Sun,[35] M. Sung,[21] P. J. Sutton,[7] G. P. Szokoly,[12] D. Talukder,[61] L. Tang,[42] D. B. Tanner,[47] S. P. Tarabrin,[25]
J. R. Taylor,[2] R. Taylor,[17] J. Thacker,[19] K. A. Thorne,[19] K. S. Thorne,[6] A. Thüring,[16] K. V. Tokmakov,[48] C. Torres,[19]
C. Torrie,[17] G. Traylor,[19] M. Trias,[44] D. Ugolini,[43] J. Ulmen,[35] K. Urbanek,[35] H. Vahlbruch,[16] M. Vallisneri,[6]
C. Van Den Broeck,[7] M. V. van der Sluys,[28] A. A. van Veggel,[48] S. Vass,[17] R. Vaulin,[60] A. Vecchio,[46] J. Veitch,[46]
P. Veitch,[45] C. Veltkamp,[2] A. Villar,[17] C. Vorvick,[18] S. P. Vyachanin,[25] S. J. Waldman,[20] L. Wallace,[17] R. L. Ward,[17]
A. Weidner,[2] M. Weinert,[2] A. J. Weinstein,[17] R. Weiss,[20] L. Wen,[6,59] S. Wen,[21] K. Wette,[4] J. T. Whelan,[1,29]
S. E. Whitcomb,[17] B. F. Whiting,[47] C. Wilkinson,[18] P. A. Willems,[17] H. R. Williams,[37] L. Williams,[47] B. Willke,[2,16]
I. Wilmut,[30] L. Winkelmann,[2] W. Winkler,[2] C. C. Wipf,[20] A. G. Wiseman,[60] G. Woan,[48] R. Wooley,[19] J. Worden,[18]
W. Wu,[47] I. Yakushin,[19] H. Yamamoto,[17] Z. Yan,[59] S. Yoshida,[33] M. Zanolin,[11] J. Zhang,[51] L. Zhang,[17] C. Zhao,[59]
N. Zotov,[22] M. E. Zucker,[20] H. zur Mühlen,[16] and J. Zweizig[17]

(LIGO Scientific Collaboration)[*]

[1]*Albert-Einstein-Institut, Max-Planck-Institut für Gravitationsphysik, D-14476 Golm, Germany*
[2]*Albert-Einstein-Institut, Max-Planck-Institut für Gravitationsphysik, D-30167 Hannover, Germany*
[3]*Andrews University, Berrien Springs, Michigan 49104, USA*
[4]*Australian National University, Canberra, 0200, Australia*
[5]*California Institute of Technology, Pasadena, California 91125, USA*
[6]*Caltech-CaRT, Pasadena, California 91125, USA*
[7]*Cardiff University, Cardiff, CF24 3AA, United Kingdom*
[8]*Carleton College, Northfield, Minnesota 55057, USA*
[9]*Charles Sturt University, Wagga Wagga, NSW 2678, Australia*
[10]*Columbia University, New York, New York 10027, USA*
[11]*Embry-Riddle Aeronautical University, Prescott, Arizona 86301, USA*
[12]*Eötvös University, ELTE 1053 Budapest, Hungary*
[13]*Hobart and William Smith Colleges, Geneva, New York 14456, USA*
[14]*Institute of Applied Physics, Nizhny Novgorod, 603950, Russia*
[15]*Inter-University Centre for Astronomy and Astrophysics, Pune - 411007, India*
[16]*Leibniz Universität Hannover, D-30167 Hannover, Germany*
[17]*LIGO–California Institute of Technology, Pasadena, California 91125, USA*
[18]*LIGO–Hanford Observatory, Richland, Washington 99352, USA*
[19]*LIGO–Livingston Observatory, Livingston, Louisiana 70754, USA*
[20]*LIGO–Massachusetts Institute of Technology, Cambridge, Massachusetts 02139, USA*
[21]*Louisiana State University, Baton Rouge, Louisiana 70803, USA*
[22]*Louisiana Tech University, Ruston, Louisiana 71272, USA*
[23]*Loyola University, New Orleans, Louisiana 70118, USA*
[24]*Montana State University, Bozeman, Montana 59717, USA*
[25]*Moscow State University, Moscow, 119992, Russia*
[26]*NASA/Goddard Space Flight Center, Greenbelt, Maryland 20771, USA*
[27]*National Astronomical Observatory of Japan, Tokyo 181-8588, Japan*
[28]*Northwestern University, Evanston, Illinois 60208, USA*
[29]*Rochester Institute of Technology, Rochester, New York 14623, USA*
[30]*Rutherford Appleton Laboratory, HSIC, Chilton, Didcot, Oxon OX11 0QX, United Kingdom*
[31]*San Jose State University, San Jose, California 95192, USA*
[32]*Sonoma State University, Rohnert Park, California 94928, USA*
[33]*Southeastern Louisiana University, Hammond, Louisiana 70402, USA*
[34]*Southern University and A&M College, Baton Rouge, Louisiana 70813, USA*
[35]*Stanford University, Stanford, California 94305, USA*
[36]*Syracuse University, Syracuse, New York 13244, USA*
[37]*The Pennsylvania State University, University Park, Pennsylvania 16802, USA*
[38]*The University of Melbourne, Parkville VIC 3010, Australia*
[39]*The University of Mississippi, University, Mississippi 38677, USA*
[40]*The University of Sheffield, Sheffield S10 2TN, United Kingdom*

[41]*The University of Texas at Austin, Austin, Texas 78712, USA*

[42]*The University of Texas at Brownsville and Texas Southmost College, Brownsville, Texas 78520, USA*

[43]*Trinity University, San Antonio, Texas 78212, USA*

[44]*Universitat de les Illes Balears, E-07122 Palma de Mallorca, Spain*

[45]*University of Adelaide, Adelaide, SA 5005, Australia*

[46]*University of Birmingham, Birmingham, B15 2TT, United Kingdom*

[47]*University of Florida, Gainesville, Florida 32611, USA*

[48]*University of Glasgow, Glasgow, G12 8QQ, United Kingdom*

[49]*University of Maryland, College Park, Maryland 20742, USA*

[50]*University of Massachusetts–Amherst, Amherst, Massachusetts 01003, USA*

[51]*University of Michigan, Ann Arbor, Michigan 48109, USA*

[52]*University of Minnesota, Minneapolis, Minnesota 55455, USA*

[53]*University of Oregon, Eugene, Oregon 97403, USA*

[54]*University of Rochester, Rochester, New York 14627, USA*

[55]*University of Salerno, 84084 Fisciano (Salerno), Italy*

[56]*University of Sannio at Benevento, I-82100 Benevento, Italy*

[57]*University of Southampton, Southampton, SO17 1BJ, United Kingdom*

[58]*University of Strathclyde, Glasgow, G1 1XQ, United Kingdom*

[59]*University of Western Australia, Crawley, Washington 6009, Australia, USA*

[60]*University of Wisconsin–Milwaukee, Milwaukee, Wisconsin 53201, USA*

[61]*Washington State University, Pullman, Washington 99164, USA*

D. P. Anderson

University of California at Berkeley, Berkeley, California 94720, USA
(Received 29 May 2009; published 11 August 2009)

This paper reports on an all-sky search for periodic gravitational waves from sources such as deformed isolated rapidly spinning neutron stars. The analysis uses 840 hours of data from 66 days of the fifth LIGO science run (S5). The data were searched for quasimonochromatic waves with frequencies f in the range from 50 to 1500 Hz, with a linear frequency drift $\dot{f}$ (measured at the solar system barycenter) in the range $-f/\tau < \dot{f} < 0.1f/\tau$, for a minimum spin-down age τ of 1000 years for signals below 400 Hz and 8000 years above 400 Hz. The main computational work of the search was distributed over approximately 100 000 computers volunteered by the general public. This large computing power allowed the use of a relatively long coherent integration time of 30 hours while searching a large parameter space. This search extends Einstein@Home's previous search in LIGO S4 data to about 3 times better sensitivity. No statistically significant signals were found. In the 125–225 Hz band, more than 90% of sources with dimensionless gravitational-wave strain tensor amplitude greater than 3×10^{-24} would have been detected.

I. INTRODUCTION

Gravitational waves (GWs) are predicted by Einstein's general theory of relativity, but have so far eluded direct detection. The Laser Interferometer Gravitational-wave Observatory (LIGO) [1,2] has been built for this purpose and is currently the most sensitive gravitational-wave detector in operation.

Rapidly rotating neutron stars are expected to generate periodic gravitational-wave signals through various mechanisms [3–9]. Irrespective of the emission mechanism, these signals are quasimonochromatic with a slowly changing intrinsic frequency. Additionally, at a terrestrial detector, such as LIGO, the data analysis problem is complicated by the fact that the periodic GW signals are

Doppler modulated by the detector's motion relative to the solar system barycenter (SSB).

A previous paper [10] reported on the results of the Einstein@Home search for periodic GW signals in the data from LIGO's fourth science run (S4). The present work extends this search, using more sensitive data from 66 days of LIGO's fifth science run (S5).

Because of the weakness of the GW signals buried in the detector noise, the data analysis strategy is critical. A powerful detection method is given by coherent matched filtering. This means one convolves all available data with a set of template waveforms corresponding to all possible putative sources. The resulting detection statistic is derived in Ref. [11] and is commonly referred to as the $\mathcal{F}$-statistic.

The parameter space to be scanned for putative signals from isolated neutron stars is four-dimensional, with two parameters required to describe the source sky position

*http://www.ligo.org/

using standard astronomical equatorial coordinates α (right ascension) and δ (declination), and additional coordinates $(f, \dot{f})$ denoting the intrinsic frequency and frequency drift, respectively. To achieve the maximum possible sensitivity, the template waveforms must match the source waveforms to within a fraction of a cycle over the entire observation time (months or years for current data samples). So one must choose a very closely spaced grid of templates in this four-dimensional parameter space. This makes the computational cost of the search very high, and therefore limits the search sensitivity [12].

To maximize the possible integration time, and hence achieve a more sensitive search, the computation was distributed via the volunteer computing project Einstein@Home [13]. This large computing power allowed the use of a relatively long coherent integration time of 30 h, despite the large parameter space searched. Thus, this search involves coherent matched filtering in the form of the $\mathcal{F}$-statistic over 30-hour-long data segments and subsequent incoherent combination of $\mathcal{F}$-statistic results via a coincidence strategy.

The methods used here are further described in Secs. II, III, and IV. Estimates of the sensitivity of this search and results are in Secs. V and VI, respectively. Previously, other all-sky searches for periodic GW sources using LIGO S4 and S5 data, which combine power from many short coherent segments (30-minute intervals) of data, have been reported by the LIGO Scientific Collaboration [14,15]. However, this Einstein@Home search explores large regions of parameter space which have not been analyzed previously with LIGO S5 data. The sensitivity of the results here are compared with previous searches in Sec. VII, and conclusions are given in Sec. VIII.

II. DATA SELECTION AND PREPARATION

The data analyzed in the present work were collected between November 19, 2005 and January 24, 2006. The total data set covering frequencies from 50 to 1500 Hz consisted of 660 h of data from the LIGO Hanford 4-km (H1) detector and 180 h of data from the LIGO Livingston 4-km (L1) detector.

The data preparation method is essentially identical to that of the previous S4 analysis [10]. Therefore only a brief summary of the main aspects is given here; further details are found in [10] and references therein. The data set has been divided into segments of 30 h each. However, the 30-hour-long data segments are not contiguous, but have time gaps. Since the number of templates required increases rapidly with observation span, the 30 h of data for each segment were chosen to lie within a time span of less than 40 h. In what follows, the notion of "segment" will always refer to one of these time stretches, each of which contains exactly $T = 30$ h of data. The total time spanned by a given data segment j is denoted by $T_{\mathrm{span},j}$ and conforms to 30 h $< T_{\mathrm{span},j} <$ 40 h.

TABLE I. Segments of early S5 data used in this search. The columns are the data segment index j, the GPS start time t_j and the time spanned $T_{\mathrm{span},j}$.

j	Detector	t_j [s]	$T_{\mathrm{span},j}$ [s]
1	H1	816 397 490	140 768
2	H1	816 778 879	134 673
3	H1	816 993 218	134 697
4	H1	817 127 915	137 962
5	H1	817 768 509	142 787
6	H1	817 945 327	143 919
7	H1	818 099 543	139 065
8	H1	818 270 501	143 089
9	H1	818 552 200	134 771
10	H1	818 721 347	138 570
11	H1	818 864 047	134 946
12	H1	819 337 064	143 091
13	H1	819 486 815	120 881
14	H1	819 607 696	116 289
15	H1	819 758 149	136 042
16	H1	820 482 173	143 904
17	H1	820 628 379	138 987
18	H1	821 214 511	126 307
19	H1	821 340 818	126 498
20	H1	821 630 884	141 913
21	H1	821 835 537	138 167
22	H1	821 973 704	142 510
23	L1	818 812 286	130 319
24	L1	819 253 562	140 214
25	L1	819 393 776	126 075
26	L1	819 547 883	138 334
27	L1	820 015 400	121 609
28	L1	821 291 797	140 758

Given the above constraints, a total of $N_{\mathrm{seg}} = 28$ data segments (22 from H1, 6 from L1) were obtained from the early S5 data considered. These data segments are labeled by $j = 1, \ldots, 28$. Table I lists the global positioning system (GPS) start time along with the time span of each segment.

In this analysis, the maximum frequency shift of a signal over the length of any given data segment and parameter-space range examined is dominated by the Doppler modulation due to the Earth's orbital motion around the SSB, while the effects of frequency change resulting from intrinsic spin-down of the source are smaller. The orbital velocity of the Earth is about $v/c \approx 10^{-4}$; hence a signal will always remain in a narrow frequency band smaller than ± 0.15 Hz around a given source frequency. Therefore, for each detector the total frequency range from 50 to 1500 Hz is broken up into 2900 slices, each of 0.5 Hz bandwidth plus overlapping wings of 0.175 Hz on either side.

The detector data contain numerous narrow-band noise artifacts, so-called "lines," which are of instrumental origin, such as harmonics of the 60 Hz mains frequency. Prior to the analysis, line features of understood origin (at the
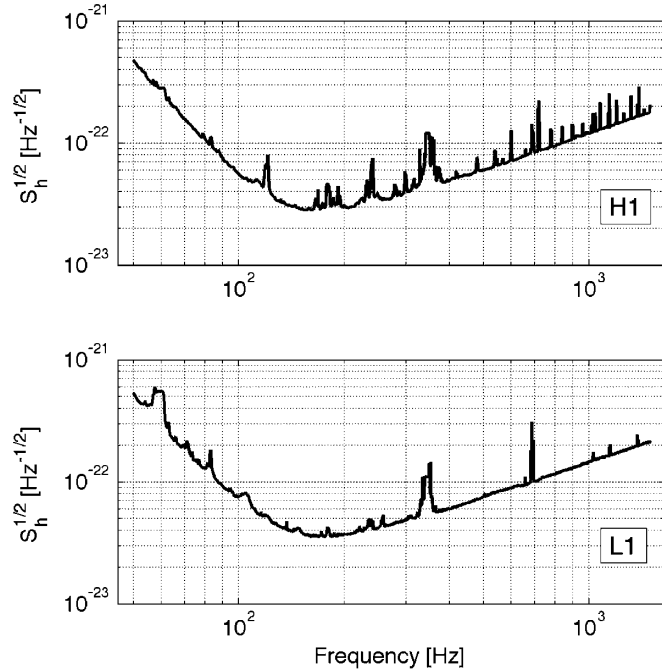
FIG. 1. Strain amplitude spectral densities $\sqrt{S_h(f)}$ of the cleaned data from the LIGO detectors H1 and L1. The curves in the top (bottom) panel are the harmonic mean of the 22 H1 (6 L1) 30-hour segments of S5 data used this Einstein@Home analysis.

time before the launch of the search) were removed ("cleaned") from the data by substitution of the frequency-domain data bins with random Gaussian noise. Table III in the appendix shows the frequencies of lines excluded from the data. The harmonic-mean noise strain amplitude spectra of the final cleaned H1 and L1 data sets are shown in Fig. 1.

III. DATA PROCESSING

The paper describing the previous Einstein@Home search in S4 data [10] presented in detail the data processing scheme. For the purpose of the present search the same data processing infrastructure is employed. Hence, here only a short summary thereof is given, pointing out the minimal changes applied in setting up the present analysis.

The total computation of the search is broken up into 16 446 454 workunits. Each workunit represents a separate computing task and is processed using the Berkeley Open Infrastructure for Network Computing (BOINC) [16–18]. To eliminate errors and weed out results that are wrong, each workunit is independently processed by at least two different volunteers. Once two successful results for a workunit are returned back to the Einstein@Home server, they are compared by an automatic validator, which discards results that differ by more than some allowed tolerance. New workunits are generated and run independently again for such cases.

In searching for periodic gravitational-wave signals, each workunit examines a different part of parameter space. A key design goal is that the computational effort to conduct the entire analysis should take about 6–7 months. An additional design goal is to minimize the download burden on the Einstein@Home volunteers' Internet connections and also on the Einstein@Home data servers. This is accomplished by letting each workunit use only a small reusable subset of the total data set, so that Einstein@Home volunteers are able to carry out useful computations on a one-day time scale.

Each workunit searches only one data segment over a narrow frequency range, but covering all of the sky and the entire range of frequency derivatives. The workunits are labeled by three indices (j, k, ℓ), where $j = 1, \ldots, 28$ denotes the data segment, $k = 1, \ldots, 2900$ labels the 0.5 Hz frequency band and $\ell = 1, \ldots, M(j, k)$ enumerates the individual workunits pertinent to data segment j and frequency band k.

In each segment the $\mathcal{F}$-statistic is evaluated on a grid in parameter space. Each parameter-space grid is constructed such that grid points (templates) are not further apart from their nearest neighbor by more than a certain distance. The distance measure is defined from a metric on parameter space, first introduced in [19,20], representing the fractional loss of squared signal-to-noise ratio (SNR^2) due to waveform mismatch between the putative signal and the template. For any given workunit, the parameter-space grid is a Cartesian product of uniformly spaced steps df in frequency, uniformly spaced steps $d\dot{f}$ in frequency derivative, and a two-dimensional sky grid, which has nonuniform spacings determined by the metric [10,21].

For frequencies in the range [50, 400) Hz, the maximal allowed mismatch was chosen as $m = 0.15$ (corresponding to a maximal loss in SNR^2 of 15%), while in the range [400, 1500) Hz, the maximal mismatch was $m = 0.4$. It can be shown [10,21] that these choices of maximal mismatch enable a coherent search of near-optimal sensitivity at fixed computational resources.

The step size in frequency f obtained from the metric depends on $T_{\text{span},j}$ of the jth data segment: $df_j = 2\sqrt{3m}/(\pi T_{\text{span},j})$. In the low-frequency range this results in frequency spacings in the range $df_j \in [2.97, 3.67]$ μHz, while for high-frequency workunits $df_j \in [4.85, 6.0]$ μHz.

The range of frequency derivatives $\dot{f}$ searched is defined in terms of the "spin-down age" $\tau \equiv -f/\dot{f}$, namely, $\tau \geq 1000$ years for low-frequency and $\tau \geq 8000$ years for high-frequency workunits. As in the S4 Einstein@Home search, these ranges were guided by the assumption that a nearby very young neutron star would correspond to a historical supernova, supernova remnant, known pulsar, or pulsar wind nebula. The search also covers a small "spin-up" range, so the actual ranges searched are $\dot{f} \in [-f/\tau, 0.1f/\tau]$. In $\dot{f}$ the grid points are spaced according

to $d\dot{f}_j = 12\sqrt{5m}/(\pi T_{\mathrm{span},j}^2)$, resulting in resolutions $d\dot{f}_j \in [1.60, 2.44] \times 10^{-10}$ Hz/s for low-frequency workunits, and $d\dot{f}_j \in [2.61, 3.99] \times 10^{-10}$ Hz/s for high-frequency workunits.

The resolution of the search grid in the sky depends on both the start time t_j and duration $T_{\mathrm{span},j}$ of the segment, as well as on the frequency f. The number of grid points on the sky scales as $\propto f^2$, and approximately as $\propto T_{\mathrm{span},j}^{2.4}$ for the range of $T_{\mathrm{span},j} \sim 30$–40 h used in this search. As was done in the previous S4 analysis [10], to simplify the construction of workunits and limit the number of different input files to be sent, the sky grids are fixed over a frequency range of 10 Hz, but differ for each data segment j. The sky grids are computed at the higher end of each 10 Hz band, so they are slightly "over-covering" the sky at lower frequencies within the band. The search covers in total a frequency band of 1450 Hz; thus there are 145 different sky grids for each data segment.

The output from one workunit in the low- (high-) frequency range contains the top 1000 (10 000) candidate events with the largest values of the $\mathcal{F}$-statistic. In order to balance the load on the Einstein@Home servers, a low-frequency workunit returns a factor of 10 fewer events, because low-frequency workunits require runtimes approximately 10 times shorter than high-frequency workunits. For each candidate event five values are reported: frequency (hertz), right ascension angle (radians), declination angle (radians), frequency derivative (hertz per second) and $2\mathcal{F}$ (dimensionless). The frequency is the frequency at the SSB at the instant of the first data point in the corresponding data segment. Returning only the "loudest" candidate events effectively corresponds to a floating threshold on the value of the $\mathcal{F}$-statistic. This avoids large lists of candidate events being produced in regions of parameter space containing non-Gaussian noise, such as instrumental artifacts that were not removed *a priori* from the input data because of unknown origin.

IV. POST-PROCESSING

After results for each workunit are returned to the Einstein@Home servers by project volunteers, post-processing is conducted on those servers and on dedicated computing clusters. The post-processing has the goal of finding candidate events that appear in many of the 28 different data segments with consistent parameters.

In this search, the post-processing methods are the same as used for the Einstein@Home S4 search [10]. Therefore, this section only summarizes the main steps; a more detailed description can be found in [10].

A consistent (coincident) set of "candidate events" is called a "candidate." Candidate events from different data segments are considered coincident if they cluster closely together in the four-dimensional parameter space. By using a grid of "coincidence cells," the clustering method can

reliably detect strong signals, which would produce candidate events with closely matched parameters in many of the 28 data segments. The post-processing pipeline operates in 0.5 Hz-wide frequency bands, and performs the following steps described below.

A. The post-processing steps

A putative source with nonzero spin-down would generate candidate events with different apparent frequency values in each data segment. To account for these effects, the frequencies of the candidate events are shifted back to the same frequency value at fiducial time t_{fiducial} via $f(t_{\mathrm{fiducial}}) = f(t_j) + (t_{\mathrm{fiducial}} - t_j)\dot{f}$, where $\dot{f}$ and $f(t_j)$ are the spin-down rate and frequency of a candidate event reported by the search code in the result file, respectively, and t_j is the time stamp of the first datum in the jth data segment. The fiducial time is chosen to be the GPS start time of the earliest ($j = 1$) data segment, $t_{\mathrm{fiducial}} = t_1 = 816\,397\,490$ s.

A grid of cells is then constructed in the four-dimensional parameter space to find coincidences among the 28 different data segments. The coincidence search algorithm uses rectangular cells in the coordinates $(f, \dot{f}, \alpha\cos\delta, \delta)$. The dimensions of the cells are adapted to the parameter-space search grid (see below). Each candidate event is assigned to a particular cell. In cases where two or more candidate events from the same data segment j fall into the same cell, only the candidate event having the largest value of $2\mathcal{F}$ is retained in the cell. Then the number of candidate events per cell coming from distinct data segments is counted, to identify cells with more coincidences than would be expected by random chance.

To ensure that candidate events located on opposite sides of a cell border are not missed, the entire cell coincidence grid is shifted by half a cell width in all possible $2^4 = 16$ combinations of the four parameter-space dimensions. Hence, 16 different coincidence-cell grids are used in the analysis.

B. Construction of coincidence windows

The coincidence cells are constructed to be as small as possible to reduce the probability of false alarms. However, since each of the 28 different data segments uses a different parameter-space grid, the coincidence cells must be chosen to be large enough that the candidate events from a source (which would appear at slightly different points in parameter space in each of the 28 data segments) would still lie in the same coincidence cell.

In the frequency direction, the size Δf for the coincidence cell is given by the largest search grid spacing in f (for the smallest value of $T_{\mathrm{span},j}$) plus the largest possible offset in spin-down: $\Delta f = \max_j(df_j + \Delta t d\dot{f}_j)$, where the maximization over j selects the data segment with the

smallest $T_{\text{span},j}$ (which is $j = 6$) and $\Delta t = |\max_j t_j - \min_j t_j| = t_{22} - t_1 = 5\,576\,214$ s is the total time span between the latest and earliest data segments. For safety, e.g. against noise fluctuations that could shift a candidate peak, Δf has been increased by a further 30%, so that the width of the coincidence cell in f below 400 Hz is $\Delta f = 1.78$ mHz and $\Delta f = 2.9$ mHz above 400 Hz.

In the frequency-derivative direction, the size of the coincidence cell is given by the largest $d\dot{f}_j$ spacing in the parameter-space grid, which is also determined by the smallest value of $T_{\text{span},j}$. For safety this is also increased by 30%, so that $\Delta\dot{f} = 3.18 \times 10^{-10}$ Hz s^{-1} below 400 Hz and $\Delta\dot{f} = 5.19 \times 10^{-10}$ Hz s^{-1} above 400 Hz.

In sky position, the size of the coincidence cells is guided by the behavior of the parameter-space metric. As described in [10], the density of grid points in the sky is approximately proportional to $|\cos(\delta)\sin(\delta)| \propto |\sin(2\delta)|$, and it follows from [10] that $\cos(\delta)d\alpha = |\sin(\delta)|d\delta = $ const. Because of the singularity when $\delta \to 0$, a useful model for the coincidence-window size varying with declination is given by

$$\Delta\alpha(\delta) = \Delta\alpha(0)/\cos(\delta),$$

$$\Delta\delta(\delta) = \begin{cases} \Delta\delta(0) & \text{if } |\delta| < \delta_c, \\ \Delta\alpha(0)/|\sin(|\delta| - \kappa\Delta\alpha(0))| & \text{if } |\delta| \geq \delta_c. \end{cases}$$

$$(1)$$

To ensure continuity at $\delta = \delta_c$, the transition point δ_c is defined by the condition $\Delta\alpha(0)/|\sin(|\delta_c| - \kappa\Delta\alpha(0))| = \Delta\delta(0)$. The tuning parameter κ is chosen based on visual inspection to be $\kappa = 1.5$ in this search. The values of $\Delta\alpha(0)$ and $\Delta\delta(0)$ are directly determined from the sky
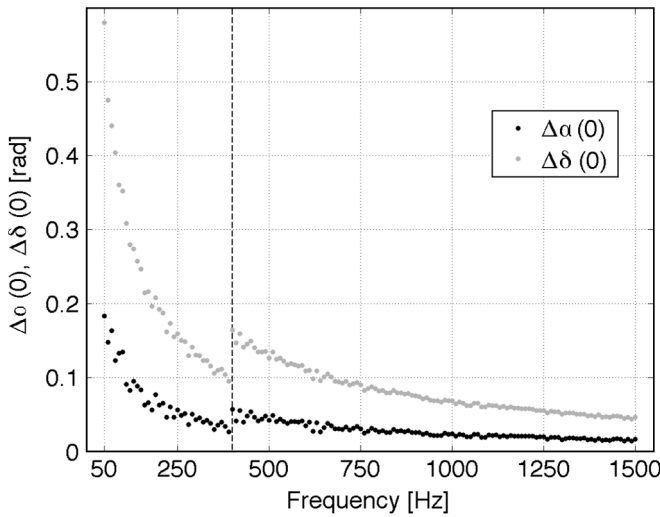

FIG. 2. The parameters $\Delta\alpha(0)$ and $\Delta\delta(0)$ of the sky coincidence-window model as a function of the 10 Hz frequency band. The vertical dashed line at 400 Hz indicates the separation between the low- and high-frequency ranges.

grids (see [10] for details). Figure 2 shows these parameters for all-sky grids as a function of frequency. As stated above, the sky grids are constant for 10 Hz-wide steps in frequency, and so these parameters vary with the same step size.

C. Output of the post-processing

The output of the post-processing is a list of the candidates with the greatest number of coincidences. The possible number of coincidences ranges from a minimum of 0 to a maximum of 28 (the number of data segments analyzed). The meaning of $\mathcal{C}$ coincidences is that there are $\mathcal{C}$ candidate events from different data segments within a given coincidence cell. In each frequency band of coincidence-window width Δf, the coincidence cell containing the largest number of candidate events is found. The pipeline outputs the average frequency of the coincidence cell, the average sky position and spin-down of the candidate events, the number of candidate events in the coincidence cell, and the "significance" of the candidate. The significance of a candidate, first introduced in [22] and explained in [10], is defined by

$$\mathcal{S} = \sum_{q=1}^{\mathcal{C}} (\mathcal{F}_q - \ln(1 + \mathcal{F}_q)), \qquad (2)$$

where $\mathcal{F}_q$ is the $\mathcal{F}$-statistic value of the qth candidate event in the same coincidence cell, which harbors a total of $\mathcal{C}$ candidate events.

D. False alarm probability and detection threshold

The central goal of this search is to make a *confident detection*, not to set upper limits with the broadest possible coverage band. This is reflected in the choice of detection threshold based on the expected false alarm rates. In this search the background level of false alarm candidates is expected at 10 coincidences (out of 28 possible). As a pragmatic choice, the threshold of confident detection is set at 20 coincidences, which is highly improbable to arise from random noise only. These settings will be elucidated in the following.

To calculate the false alarm probabilities, consider the case where $\mathcal{E}_{\text{seg}}(k)$ candidate events per data segment obtained from pure Gaussian noise are distributed uniformly about $N_{\text{cell}}(k)$ independent coincidence cells in a given 0.5 Hz band k. Assuming the candidate events are independent, the probability $p_F(k; \mathcal{C}_{\max})$ per coincidence cell of finding $\mathcal{C}_{\max}$ or more candidate events from different data segments has been derived in [10] and is given by the binomial distribution

$$p_F(k; \mathcal{C}_{\max}) = \sum_{n=\mathcal{C}_{\max}}^{N_{\text{seg}}} \binom{N_{\text{seg}}}{n} [\epsilon(k)]^n [1 - \epsilon(k)]^{N_{\text{seg}} - n}, \quad (3)$$

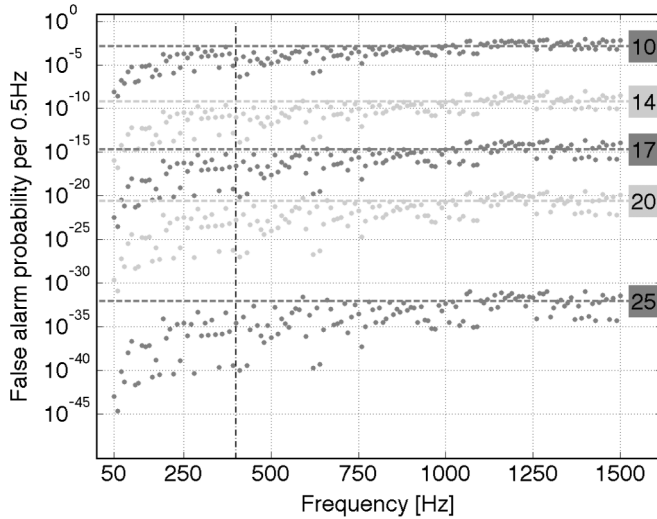FIG. 3. False alarm probabilities $P_F(k; \mathcal{C}_{max})$ as a function of frequency band (labeled by k) for different values of $\mathcal{C}_{max} \in \{10, 14, 17, 20, 25\}$. The dashed horizontal lines represent the corresponding average across all frequencies. The vertical dashed line at 400 Hz indicates the separation between the low- and high-frequency ranges.

where $\epsilon(k)$ denotes the probability of populating any given coincidence cell with one or more candidate events in a given data segment, obtained as

$$\epsilon(k) = 1 - \left(1 - \frac{1}{N_{cell}(k)}\right)^{\mathcal{E}_{seg}(k)}. \qquad (4)$$

Finally, the probability $P_F(k; \mathcal{C}_{max})$ that there are $\mathcal{C}_{max}$ or more coincidences in *one or more* of the N_{cell} cells per 0.5 Hz band k is

$$P_F(k; \mathcal{C}_{max}) = 1 - [1 - p_F(k; \mathcal{C}_{max})]^{N_{cell}}. \qquad (5)$$

Figure 3 shows the dependence of $P_F(k; \mathcal{C}_{max})$ on the frequency bands for different values of $\mathcal{C}_{max}$. One finds that the average false alarm probability of obtaining 10 or more coincidences is approximately 10^{-3}. This means, in our analysis of 2900 half-Hz frequency bands, only a few candidates are expected to have 10 or more coincidences. Thus this will be the anticipated background level of coincidences, because from pure random noise one would not expect candidates of *more than* 10 coincidences in this analysis. In contrast, the false alarm probability of reaching the detection threshold of 20 or more coincidences per 0.5 Hz averaged over all frequency bands is about 10^{-21}. Therefore, this choice of detection threshold makes it extremely improbable to be exceeded in the case of random noise.

During parts of the LIGO S5 run ten simulated periodic GW signals were injected at the hardware level by modulating the interferometer mirror positions via signals sent to voice actuation coils surrounding magnets glued near the mirror edges. The hardware injections were scheduled with an overall duty cycle of about 50% during S5 to minimize potential interference for other GW searches. Thus, in only 12 (of the 28) data segments chosen for this search were these hardware injections active more than 90% of the time. Therefore, the hardware injections are not expected to meet the detection condition defined above, simply because they were inactive during a large fraction of the data used in this analysis. For future science runs improved understanding will allow the hardware injections to be activated permanently.

V. ESTIMATED SENSITIVITY

The methods used here would be expected to yield very high confidence if a strong signal were present. To estimate the sensitivity of this detection scheme, Monte Carlo methods are used to simulate a population of sources. The goal is to find the strain amplitude h_0 at which 10%, 50%, or 90% of sources uniformly populated over the sky and in their "nuisance parameters" would be confidently detected. In this analysis, "detectable" means "produces coincident events in 20 or more distinct data segments." As discussed above, the false alarm probability for obtaining such a candidate in a given 0.5 Hz band is of order 10^{-21}. This is therefore an estimate of the signal strength required for high-confidence detection. For this purpose, the pipeline developed in [10] is run here, using the input data of the present analysis. A large number of distinct simulated sources (trials) are tested for detection. A "trial" denotes a single simulated source which is probed for
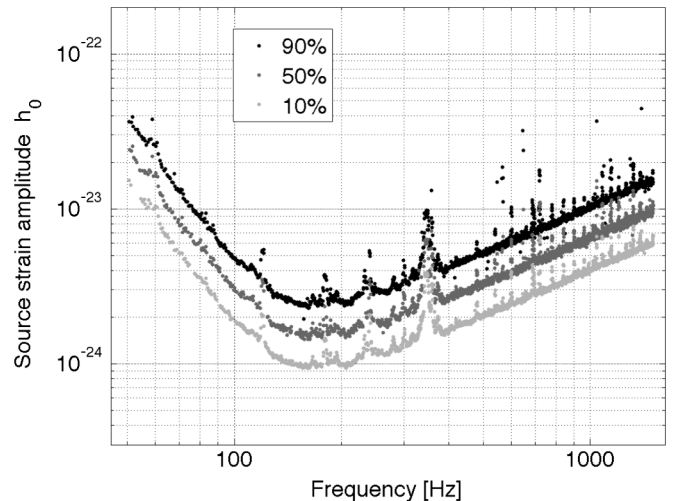

FIG. 4. Estimated sensitivity of the Einstein@Home search for isolated periodic GW sources in the early S5 LIGO data. The set of three curves shows the source strain amplitudes h_0 at which 10% (bottom), 50% (middle) and 90% (top) of simulated sources would be confidently detected (i.e., would produce at least 20 coincidences out of 28 possible) in this Einstein@Home search.

detection. For a detailed description of the methodology, the reader is referred to [10].

Figure 4 shows the resulting search sensitivity curves as functions of frequency. Each data point on the plot denotes the results of 1000 independent trials. These show the values of h_0 as defined in [11] such that 10%, 50%, and 90% of simulated sources are confidently detected in the post-processing pipeline.

The dominant sources of error in these sensitivity curves are uncertainties in calibration of the LIGO detector response functions (cf. [10,15]). The uncertainties range typically from about 8% to 15%, depending on frequency.

The behavior of the curves shown in Fig. 4 essentially reflects the instrument noise given in Fig. 1. One may fit the curves obtained in Fig. 4 to the shape of the harmonic-mean averaged strain noise power spectral density $S_h(f)$. Then the three sensitivity curves in Fig. 4 are described by

$$h_0^{\mathcal{D}}(f) \approx R_{\mathcal{D}}\sqrt{\frac{S_h(f)}{30 \text{ h}}}, \qquad (6)$$

where the prefactors $R_{\mathcal{D}}$ for different detection probabilities levels $\mathcal{D} = 90\%$, 50% and 10% are well fit below 400 Hz by $R_{90\%} = 29.4$, $R_{50\%} = 18.5$, and $R_{10\%} = 11.6$, and above 400 Hz by $R_{90\%} = 30.3$, $R_{50\%} = 19.0$, and $R_{10\%} = 11.8$.

VI. RESULTS

A. Vetoing instrumental-noise lines

At the time the instrument data were prepared and cleaned, narrow-band instrumental line features of known origin were removed, as previously described in Sec. II. However, the data also contained stationary instrumental line features that were not understood, or were poorly understood, and thus were not removed *a priori*. After the search had been conducted, at the time the post-processing started, the origin of more stationary noise lines became known. Therefore, these lines, whose origin was tracked down after the search, are excluded (cleaned *a posteriori*) from the results. A list of the polluted frequency bands which have been cleaned *a posteriori* is shown in Table IV in the appendix.

However, noise features still not understood instrumentally at this point were not removed from the results. As a consequence, the output from the post-processing pipeline contains instrumental artifacts that in some respects mimic periodic GW signals. But these artifacts tend to cluster in certain regions of parameter space, and in many cases they can be automatically identified and vetoed as done in previous searches [10,24]. The method used here is derived in [23] and a detailed description of its application is found in [10].

For a coherent observation time baseline of 30 h the parameter-space regions where instrumental lines tend to appear are determined by global-correlation hypersurfaces [23] of the $\mathcal{F}$-statistic. On physical grounds, in these parameter-space regions there is little or no frequency Doppler modulation from the Earth's motion, which can lead to a relatively stationary detected frequency. Thus, the locations of instrumental-noise candidate events are described by

$$\left| \dot{f} + f\frac{\mathbf{v}_j}{c} \cdot \hat{\mathbf{n}} \right| < \epsilon, \qquad (7)$$

where c denotes the speed of light, $\hat{\mathbf{n}}$ is a unit vector pointing to the source's sky location in the SSB frame and relates to the equatorial coordinates α and δ by $\hat{\mathbf{n}} = (\cos\delta\cos\alpha, \cos\delta\sin\alpha, \sin\delta)$, and $\mathbf{v}_j$ is the orbital velocity of the Earth at the midpoint of the jth data segment ($|\mathbf{v}_j| \approx 10^{-4}c$). The parameter ϵ accounts for a certain tolerance needed due to the parameter-space gridding and can be understood as $\epsilon = \Delta f/N_c\Delta T$, where Δf denotes width in frequency (corresponding to the coincidence-cell width in the post-processing) up to which candidate events can be resolved during the characteristic length of time ΔT, and N_c represents the size of the vetoed or rejected region, measured in coincidence cells. In this analysis $\Delta T = 5\,718\,724$ s (≈ 66 days) is the total time interval spanned by the input data.

Because false alarms are expected at the level of 10 coincidences, candidates that satisfy Eq. (7) for more than 10 data segments are eliminated (vetoed). The fraction of parameter space excluded by this veto is determined by Monte Carlo simulations to be about 13%. From Eq. (7) it follows that for fixed frequency the resulting fraction of sky excluded by the veto (uniformly averaged over spin-down) is greatest at lowest frequencies and decreases approximately as f^{-1} for higher frequencies. Appendix A of Ref. [10] presents an example calculation, illustrating the parameter-space volume excluded by this vetoing method.

B. Post-processing results

Figures 5 and 6 summarize all post-processing results from the entire search frequency range of 50 to 1500 Hz, for each frequency coincidence cell maximized over the entire sky and full spin-down range.

In Fig. 5(a) all candidates that have 7 or more coincidences are shown in a sky projection. The color scale is used to indicate the number of coincidences. The most prominent feature still apparent forms an annulus of high coincidences in the sky, including the ecliptic poles, a distinctive fingerprint of the instrumental-noise lines [23]. To obtain the results shown in Fig. 5(b), the set of candidates is cleaned *a posteriori* by removing strong instrumental-noise lines, whose origin became understood after the search was begun, and excluding the hardware injections. Finally, in Fig. 5(c) the parameter-space veto is
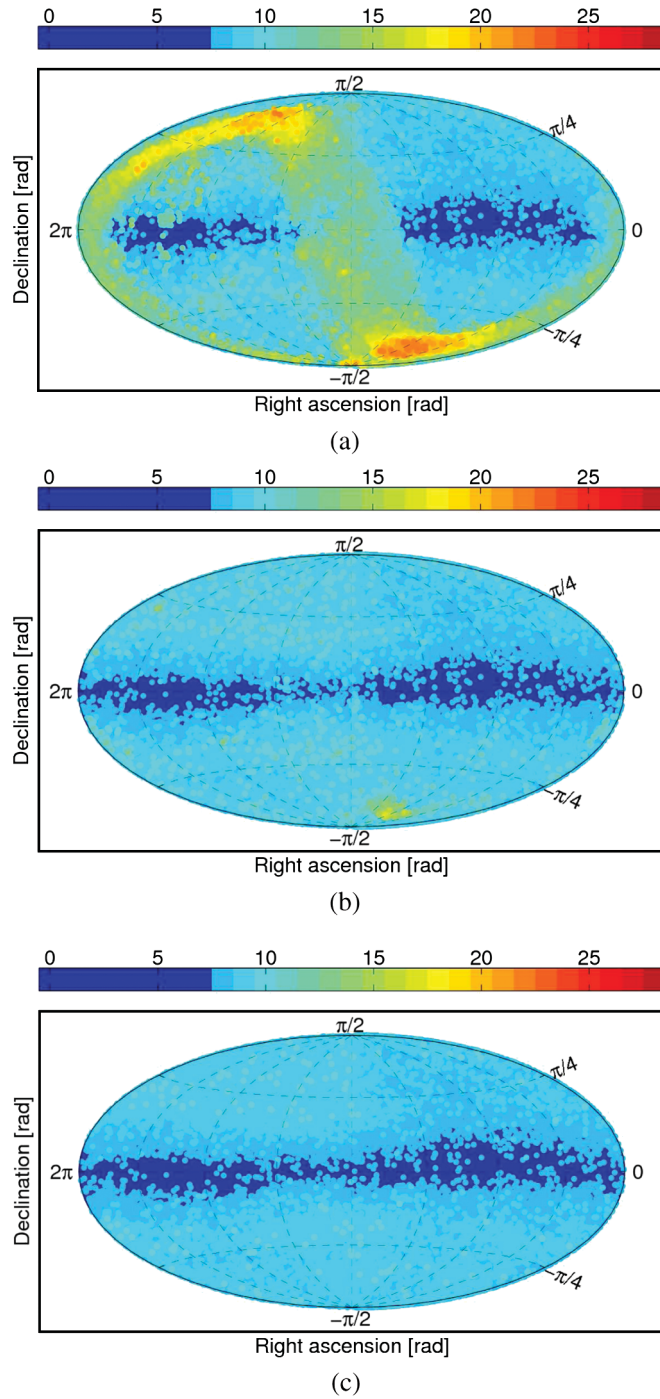
(a)

(b)

(c)

FIG. 5 (color). Sky maps of post-processing results. Candidates having more than 7 coincidences are shown in Hammer-Aitoff projections of the sky. The color bar indicates the number of coincidences of a particular candidate (cell). The top plot (a) shows the coincidence analysis results. In (b), *a posteriori* strong lines of known instrumental origin and hardware injections are removed. The bottom plot (c) is obtained by additionally applying the parameter-space veto and excluding single-detector candidates. Note that in every sky map the regions of lower coincidences near the equatorial plane (colored dark blue) are due to the sky-grid construction (cf. Fig. 3 in [10]).
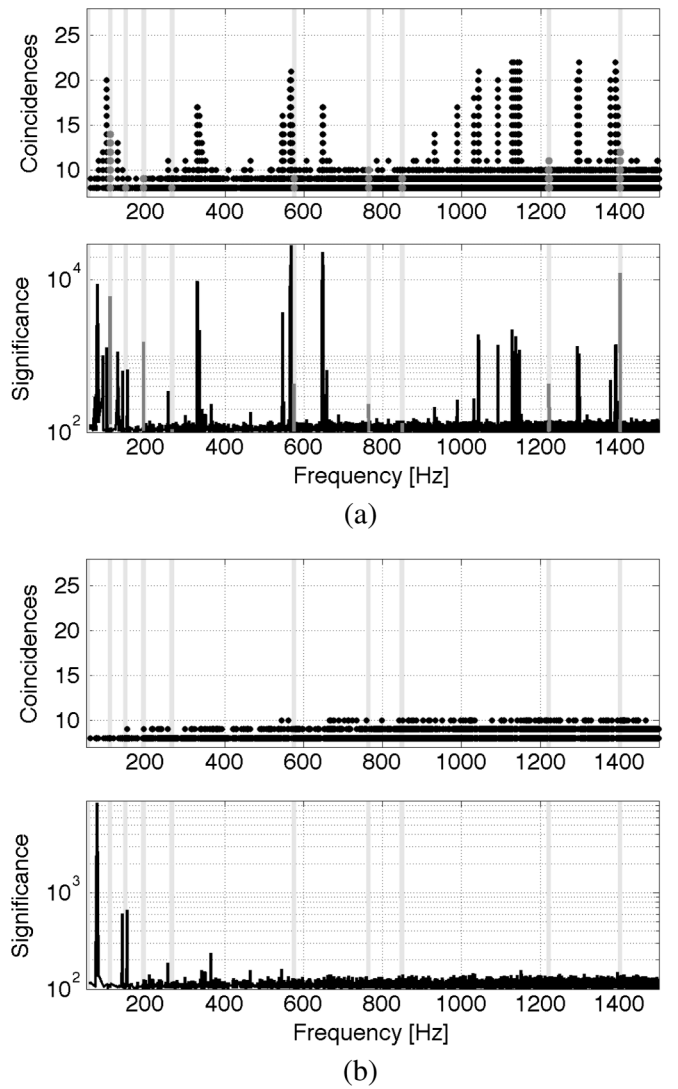

(a)

(b)

FIG. 6. The top plot (a) shows the post-processing candidates having more than 7 coincidences as function of frequency. The light-gray shaded rectangular regions highlight the frequency bands of the hardware injections. The dark-gray data points show the candidates resulting from the hardware-injected GW signals. In (b), the final results are shown after exclusion of instrumental lines of known origin and hardware injections, application of parameter-space veto and exclusion of single-detector candidates.

applied and coincidence cells which contain candidate events from a single detector only are excluded, too.

In Fig. 6(a) the coincidences and significance of all candidates that have 7 or more coincidences are shown as a function of frequency. From this set of candidates the hardware injections are excluded, strong instrumental-noise lines of known origin are removed, the parameter-space veto is applied and finally single-detector candidates are excluded to obtain Fig. 6(b).

As can be seen from Figs. 5(c) and 6(b) there are no candidates that exceed the predefined detection threshold

TABLE II.   The ten most significant post-processing candidates that have 10 or more coincidences. The frequency of each candidate f_{cand} refers to the fiducial GPS time $t_{\mathrm{fiducial}} = 816\,397\,490$ s. The parameters δ_{cand}, α_{cand}, $\dot{f}_{\mathrm{cand}}$, $\mathcal{C}_{\mathrm{cand}} = \mathcal{C}^{\mathrm{H1}}_{\mathrm{cand}} + \mathcal{C}^{\mathrm{L1}}_{\mathrm{cand}}$ and $\mathcal{S}_{\mathrm{cand}}$ are for the most-significant, most-coincident candidate with the given frequency of f_{cand}, where $\mathcal{C}^{\mathrm{H1}}_{\mathrm{cand}}$ and $\mathcal{C}^{\mathrm{L1}}_{\mathrm{cand}}$ denote the number of coincidences from detectors H1 and L1, respectively.

f_{cand} [Hz]	δ_{cand} [rad]	α_{cand} [rad]	$\dot{f}_{\mathrm{cand}}$ [Hz s^{-1}]	$\mathcal{C}_{\mathrm{cand}}$	$\mathcal{C}^{\mathrm{H1}}_{\mathrm{cand}}$	$\mathcal{C}^{\mathrm{L1}}_{\mathrm{cand}}$	$\mathcal{S}_{\mathrm{cand}}$	P_{F} per 0.5 Hz
543.810 438	0.6823	5.9944	-3.24×10^{-10}	10	8	2	160.9	7.2×10^{-5}
1151.534 608	1.1330	5.4462	2.11×10^{-11}	10	4	6	154.3	1.4×10^{-3}
1395.351 068	-1.1928	2.5980	-3.92×10^{-9}	10	8	2	150.4	7.1×10^{-4}
1249.855 062	-1.2380	6.0203	-2.43×10^{-9}	10	8	2	144.2	4.5×10^{-3}
1311.458 030	-0.5143	6.1638	-3.32×10^{-9}	10	8	2	142.8	1.7×10^{-3}
1033.967 720	0.6002	5.3133	-1.83×10^{-9}	10	8	2	142.7	1.2×10^{-3}
851.799 376	1.1071	3.2019	-7.79×10^{-10}	10	8	2	142.1	4.1×10^{-4}
665.944 644	-0.4602	2.3638	-1.28×10^{-9}	10	6	4	141.9	1.0×10^{-3}
669.187 638	-0.6928	3.0333	-1.58×10^{-9}	10	7	3	141.6	1.0×10^{-3}
1443.831 722	0.7046	6.0788	-4.47×10^{-9}	10	7	3	141.5	3.5×10^{-3}

of 20 coincidences (which would initiate a more extensive investigation). The largest number of coincidences found is 10, which is at the background level of false alarms expected from random noise only. From these candidates having 10 coincidences, Table II lists the ten most significant ones.

VII. COMPARISON WITH PREVIOUS SEARCHES

A previous paper [10] reported on the results of the Einstein@Home search for periodic GW signals in the LIGO S4 data. The present work extends this search analyzing more sensitive LIGO S5 data while using the same methods described in [10]. Therefore, this section elucidates the changes in configuration of the search and post-processing.

First, not only are more sensitive data used here, but also a larger total volume of data is searched compared to [10]. The number of 30-hour data segments analyzed increased from 17 to 28.

In addition, the template grids used in each data segment of this search were constructed to be denser, reducing the possible loss of signals due to mismatch in the template waveforms. Compared to the previous search in S4 data, where a maximal mismatch of $m = 0.2$ ($m = 0.5$) was used in the low- (high-) frequency range, here templates are placed on a grid of higher density using $m = 0.15$ ($m = 0.4$) in the low- (high-) frequency range.

Moreover, in the high-frequency range a larger range of possible spin-downs is searched. The S4 analysis searched over minimum spin-down ages greater than 10 000 yr for frequencies in the higher range ($f > 300$ Hz), whereas this analysis searches over minimum spin-down ages greater than 8000 yr for frequencies in the higher range ($f > 400$ Hz). The different partitioning of frequencies into the low and high ranges (split at 300 Hz in S4, split at 400 Hz here) is a consequence of an optimization study reflecting the overall most sensitive search at given computing power.

This search presented here analyzed in total about 3 times more workunits than in the S4 search. In searching the S4 data, each workunit returned the top 13 000 candidate events, whereas this search is designed to keep only the top 1000 (10 000) candidate events in the low- (high-) frequency range. This configuration has the purpose of balancing the load on the Einstein@Home servers, which receive the workunit results. A low-frequency workunit returns a factor of 10 fewer events, because these were designed to last approximately 10 times less than each high-frequency workunit.

Finally, based on the estimates presented in Sec. V, the present search is overall about a factor of 3 more sensitive than the previous S4 search. This improvement is a consequence of using more sensitive detector data in combination with a finer-spaced template bank.
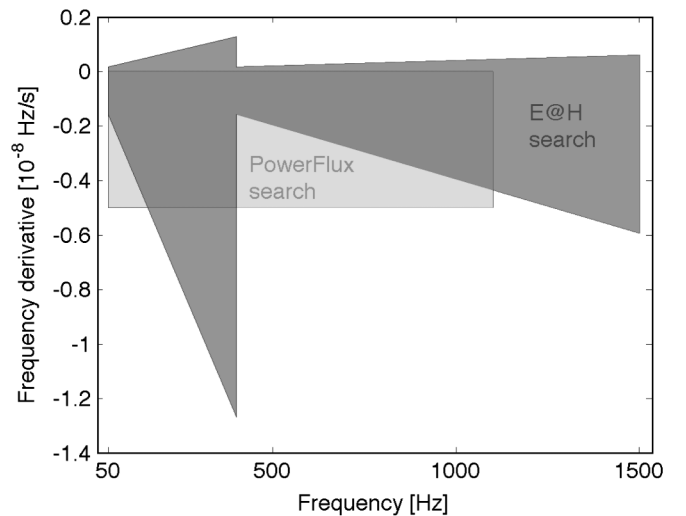

FIG. 7.   Comparison of search parameter spaces in the plane of frequency and frequency derivative. The dark-gray region refers to this Einstein@Home all-sky analysis in early S5 LIGO data. The light-gray area corresponds to the recent all-sky PowerFlux search [15] in early S5 LIGO data.

The methods used here, as well as in the S4 paper, would be expected to give very high confidence if a strong enough signal were present in the data. It is interesting to compare the sensitivity of this detection scheme with the sensitivity of upper limits such as presented recently in [15]. Based on the PowerFlux method [24], that analysis set strain upper limits at the 95% confidence level in the frequency range of 50–1100 Hz and the frequency-derivative range of -5×10^{-9}–0 Hz s^{-1} using 7147 h of early S5 LIGO data, about 8.5 times more data than were used here. Note that this Einstein@Home search explores substantially larger parts of parameter space in frequency and frequency derivative, as shown in Fig. 7.

The upper-limit worst-case results of [15] for the equatorial sky region are remarkably close to the 90%-detection-level h_0 values of Fig. 4. However, these PowerFlux upper limits refer to the most unfavorable polarization and sky position. A population-based upper limit over all sky locations and polarizations would be lower.

On the other hand, another key difference between the PowerFlux upper limits procedure and the sensitivity estimation carried out here is the detection criteria. In the present work, detection requires a signal to generate 20 or more coincidences among the 28 different data segments. This corresponds to a false alarm probability in Gaussian noise of the order 10^{-21} per 0.5 Hz frequency band. This is different from [15], where simulated signals are compared to the strongest candidates found. Thus, an equivalent detection criterion for this work would be to compare the signals against the strongest candidates in each 0.5 Hz band. These are typically 10 coincidences, which relates to a Gaussian noise false alarm rate of order 10^{-3}. One can estimate the effect on sensitivity by recomputing the sensitivity estimation of Sec. V, but requiring each signal to produce only 10 coincidences. This reduces the prefactors $R_{\mathcal{D}}$ given above by a factor of 1.24.

Apart from the larger parameter space searched, the present analysis is achieving roughly comparable sensitivity to [15] in spite of searching 8.5 times less data. Much of this effectiveness is due to the increased coherent integration time (30 hours versus 30 minutes), which is only possible due to the great amount of computing power donated by the tens of thousands of Einstein@Home volunteers.

VIII. CONCLUSION

Using early fifth-science-run LIGO data this paper reports on the results from the Einstein@Home search for unknown periodic GW sources, extending the previous Einstein@Home search in LIGO S4 data [10]. The sensitivity of the present analysis improves upon the previous Einstein@Home S4 search by a factor of about 3. Additionally, in large regions of the parameter space

probed, this analysis yields the currently most sensitive all-sky search results for periodic GW sources.

No credible periodic GW signal was found. Over a 100 Hz-wide band around the detectors' most sensitive frequencies, more than 90% of sources with dimensionless gravitational-wave strain amplitude greater than 3×10^{-24} would have been detected.

While no statistically significant signal was observed in this analysis, the results demonstrate the capability of public distributed computing to accomplish a sensitive periodic GW search for the benefit of future searches.

The sensitivity of the present analysis is essentially limited by the first-stage threshold on $\mathcal{F}$-statistics forced by the limited data volume which can be returned from the participating clients. A new Einstein@Home search currently underway carries out the incoherent combination of $\mathcal{F}$-statistic results on the client machines (done here in the post-processing once results were sent back). This makes it possible to set a much lower (sensitivity-optimized) first-stage threshold on $\mathcal{F}$-statistics. Hence, results from the new search promise a significant enhancement in the overall sensitivity for a periodic GW detection.

APPENDIX: CLEANED INSTRUMENTAL-NOISE LINES

Table III lists the frequencies of noise lines excluded from the data and replaced by Gaussian noise *a priori* to

TABLE III. Instrumental-noise lines cleaned from H1 and L1 data. The three columns show the central frequency f_{Line}, the bandwidth $\Delta f_{\text{Line}}^{(1)}$ removed below the central frequency and the bandwidth $\Delta f_{\text{Line}}^{(2)}$ removed above the central frequency. Thus the total bandwidth removed per central frequency is $\Delta f_{\text{Line}}^{(1)} + \Delta f_{\text{Line}}^{(2)}$. In addition, at *each harmonic* of the 60 Hz mains frequency, the same bandwidth is also removed. A zero bandwidth indicates that the line-cleaning algorithm replaces in these cases a single Fourier bin with the average of bins on either side. The spacing between Fourier bins is $1/1800$ Hz.

H1

f_{Line} [Hz]	$\Delta f_{\text{Line}}^{(1)}$ [Hz]	$\Delta f_{\text{Line}}^{(2)}$ [Hz]
46.7	0.0	0.0
60.0	1.0	1.0
346.0	4.0	4.0
393.1	0.0	0.0
686.9	0.3	0.3
688.2	0.3	0.3
689.5	0.5	0.6
694.75	1.25	1.25
1030.55	0.1	0.1
1032.18	0.04	0.04
1032.58	0.1	0.1
1033.7	0.1	0.1
1033.855	0.05	0.05
1034.6	0.4	0.4
1041.23	0.1	0.1
1042.0	0.5	0.2
1043.4	0.2	0.2
1144.3	0.0	0.0
1373.75	0.1	0.1
1374.44	0.1	0.1
1377.14	0.1	0.1
1378.75	0.1	0.1
1379.52	0.1	0.1
1389.06	0.06	0.06
1389.82	0.07	0.07
1391.5	0.2	0.2
54.7	0.0	0.0
60.0	1.0	1.0
345.0	5.0	5.0
396.7	0.0	0.0
686.5	1.0	1.0
688.83	0.5	0.5
693.7	0.7	0.7
1029.5	0.25	0.25
1031	0.5	0.5
1033.6	0.2	0.2
1041	1.0	1.0
1151.5	0.0	0.0
1372.925	0.075	0.075
1374.7	0.1	0.1
1375.2	0.1	0.1
1378.39	0.1	0.1
1387.4	0.05	0.05
1388.5	0.3	0.3

the search. Table IV lists the central frequencies around either side of which the Doppler band ($\Delta f_{\text{Line}} = f_{\text{Line}} \times 10^{-4}$) is *a posteriori* excluded from the postprocessed search results.

TABLE IV. Frequencies of instrumental lines that have been excluded *a posteriori* from the post-processed search results. Each column shows the central frequency f_{Line} around which a bandwidth of $\Delta f_{\text{Line}} = f_{\text{Line}} \times 10^{-4}$ has been removed on either side. The cleaned bandwidth corresponds to the maximum possible frequency shift due to the global parameter-space correlations [23]. On physical grounds this is related to the maximum possible Doppler shift due to the orbital velocity of the Earth, which is approximately 10^{-4} in units of the speed of light.

f_{Line} [Hz]	f_{Line} [Hz]	f_{Line} [Hz]	f_{Line} [Hz]
69.75	568.17	1030.55	1292.91
90.0	570.41	1042.19	1294.14
100.0	645.56	1043.33	1297.67
128.0	646.46	1092.01	1298.93
256.0	647.07	1128.28	1317.47
335.0	648.84	1132.22	1377.14
329.0	649.46	1136.23	1388.38
546.01	658.74	1142.87	1390.70
548.38	686.92	1145.29	1391.60
564.14	930.34	1146.59	
566.17	988.19	1291.11	

[1] A. Abramovici *et al.*, Science **256**, 325 (1992).

[2] B. C. Barish and R. Weiss, Phys. Today **52**, 44 (1999).

[3] L. Bildsten, Astrophys. J. **501**, L89 (1998).

[4] B. J. Owen, L. Lindblom, C. Cutler, B. F. Schutz, A. Vecchio, and N. Andersson, Phys. Rev. D **58**, 084020 (1998).

[5] G. Ushomirsky, C. Cutler, and L. Bildsten, Mon. Not. R. Astron. Soc. **319**, 902 (2000).

[6] C. Cutler, Phys. Rev. D **66**, 084025 (2002).

[7] D. I. Jones and N. Andersson, Mon. Not. R. Astron. Soc. **331**, 203 (2002).

[8] A. Melatos and D. J. B. Payne, Astrophys. J. **623**, 1044 (2005).

[9] B. J. Owen, Phys. Rev. Lett. **95**, 211101 (2005).

[10] B. Abbott *et al.* (LIGO Scientific Collaboration), Phys. Rev. D **79**, 022001 (2009).

[11] P. Jaranowski, A. Królak, and B. F. Schutz, Phys. Rev. D **58**, 063001 (1998).

[12] P. Jaranowski and A. Królak, Phys. Rev. D **61**, 062001 (2000).

[13] http://einstein.phys.uwm.edu.

[14] B. Abbott *et al.* (LIGO Scientific Collaboration), Phys. Rev. D **77**, 022001 (2008).

[15] B. Abbott *et al.* (LIGO Scientific Collaboration), Phys. Rev. Lett. **102**, 111102 (2009).

[16] The Einstein@Home project is built upon the BOINC architecture described at http://boinc.berkeley.edu/.

[17] D. P. Anderson, in *GRID '04: Proceedings of the Fifth IEEE/ACM International Workshop on Grid Computing* (IEEE Computer Society, Washington, DC, 2004), pp. 4–10.

[18] D. P. Anderson, C. Christensen, and B. Allen, in *SC '06: Proceedings of the 2006 ACM/IEEE Conference on Supercomputing* (Association for Computing Machinery, New York, 2006), p. 126.

[19] R. Balasubramanian, B. S. Sathyaprakash, and S. V. Dhurandhar, Phys. Rev. D **53**, 3033 (1996).

[20] B. J. Owen, Phys. Rev. D **53**, 6749 (1996).

[21] B. Krishnan, B. J. Owen, R. Prix, and A. M. Sintes, LIGO Report No. LIGO-T080340, 2008, available at http://admdbsrv.ligo.caltech.edu/dcc/.

[22] B. Abbott *et al.* (LIGO Scientific Collaboration), Phys. Rev. D **76**, 082001 (2007).

[23] H. J. Pletsch, Phys. Rev. D **78**, 102005 (2008).

[24] B. Abbott *et al.* (LIGO Scientific Collaboration), Phys. Rev. D **77**, 022001 (2008).